Nanoscale Advances

ROYAL SOCIETY OF CHEMISTRY

COMMUNICATION

View Article Online
View Journal | View Issue



Cite this: *Nanoscale Adv.*, 2020, **2**, 2720

Received 17th April 2020
Accepted 18th May 2020

DOI: 10.1039/d0na00304b

rsc.li/nanoscale-advances

# Beam generation and structural optimization of size-selected $Au_{923}$ clusters

Siqi Lu,†[ab] Kuojuei Hu,†[ab] Zewen Zuo,[ab] Shengyong Hu,[ab] Guanghou Wang,[ab] Fengqi Song *[ab] and Lu Cao*[ab]

A size-selected beam of $Au_{923\pm20}$ clusters is generated in a gas-phase condensation cluster source equipped with a lateral time-of-flight mass selector. The beam current reaches up to 9.13 nA for small clusters and 80 pA for $Au_{923\pm20}$ clusters, which are then analyzed using a scanning transmission electron microscope. Four types of metastable structures are observed for the $Au_{923\pm20}$ clusters, including inodecahedron (Dh), cuboctahedron and icosahedron (Ih). The proportion of bulk-favorable cuboctahedron (*i.e.* face center cubic (Fcc)) structure takes up only 10–20%, while the penta-rotating symmetrical structures (Dh/Ih) are the dominant ones which take up over three quarters. Changing the beam condition may optimize the clusters from Dh-dominant to the Ih-dominant phase, which paves the way towards nanoparticle control beyond the diameters.

Clusters are a series of materials composed of several to hundreds of atoms. The limited atom numbers and large specific surface area indicate that clusters cannot easily form periodical structures and can show numerous other structures.[1–3] Finding new structures is the fundamental task of the cluster science, based on which numerous novel properties have been discovered.[4,5] One of the attractive element is gold. Due to the strong relativistic effect, the decrease in the energy of the 6s electron and the increase in that of the 5d electrons along with s-d hybridization occur in gold,[6,7] playing a key role in the formation of novel structures, such as cages,[8] planar structures,[7] Dh, Ih[5] and tetrahedron.[9] The evolution of the cluster structure of gold with respect to size/atomic number,[10,11] temperature,[12,13] substrates[14,15] and even gas environments[16] has been studied in detail, but only few studies commit to the directional structure control of these clusters.[17] The precise control of the cluster structural transformation with certain atomic numbers and high yield are of great importance for the precise study of properties and further practical applications. Not only catalysis[18] but optical nanoclusters[19] also require the precise controlled clusters with both atomic number and nanostructure precision.

$Au_{923}$ is a magic number cluster[20] with sufficient yield in our experiment. The structures of the as-prepared $Au_{923}$ through a magnetron sputtering cluster source in STEM include Dh, Fcc and Ih.[21] The direct structure control of such a big cluster from the original Au atoms will be of great importance beyond the size control, which has been achieved for a long time. Here, we study the structural optimization of the size-selected $Au_{923}$ clusters through our magnetron sputtering cluster source. The original highest proportion of the Dh structure with considerable yield can be conversed to another penta-rotating symmetrical Ih structure with proper conditions; however, the bulk-favorite Fcc structure remains only a little part between 10% and 20%.

A magnetron sputtering gas-phase condensation cluster source equipped with a lateral time-of-flight mass selector[22,23] is used for cluster preparation and its schematic is shown in Fig. 1(a). Clusters with a mass resolution of about 4% can be produced. The process of cluster formation is shown in Fig. 1(b). Energetic gold atoms are sputtered out by bombarding the gold target with ionized argon atoms and then cooled down through the multi-body collision with He atoms.[24,25] Then, the cooled Au atoms aggregate with each other and gradually grow up. By controlling the collision time we can enrich clusters within a certain atomic number range. The as-prepared clusters finally soft-land on ultrathin carbon films. The morphology and size of the as-synthesized $Au_{923\pm20}$ clusters are studied using a spherical-aberration-corrected STEM, carried out on an FEI Themis Z at the National Graphene Center in Wuxi, China. In order to diminish the statistical error for size and structural statistics, over 50 images are collected for each group of clusters under different synthesis conditions. Four types of structures are observed, including Dh, Fcc, Ih and an unknown structure, which cannot be classified due to the blurred image. To classify the structures, the simulated STEM image atlas of each possible

[a]National Laboratory of Solid State Microstructures, Collaborative Innovation Center of Advanced Microstructures, School of Physics, Nanjing University, Nanjing 210093, China. E-mail: songfengqi@nju.edu.cn; caolu@nju.edu.cn

[b]Atomic Manufacture Institute (AMI), 211805 Nanjing, China

† These authors contributed equally to this work.

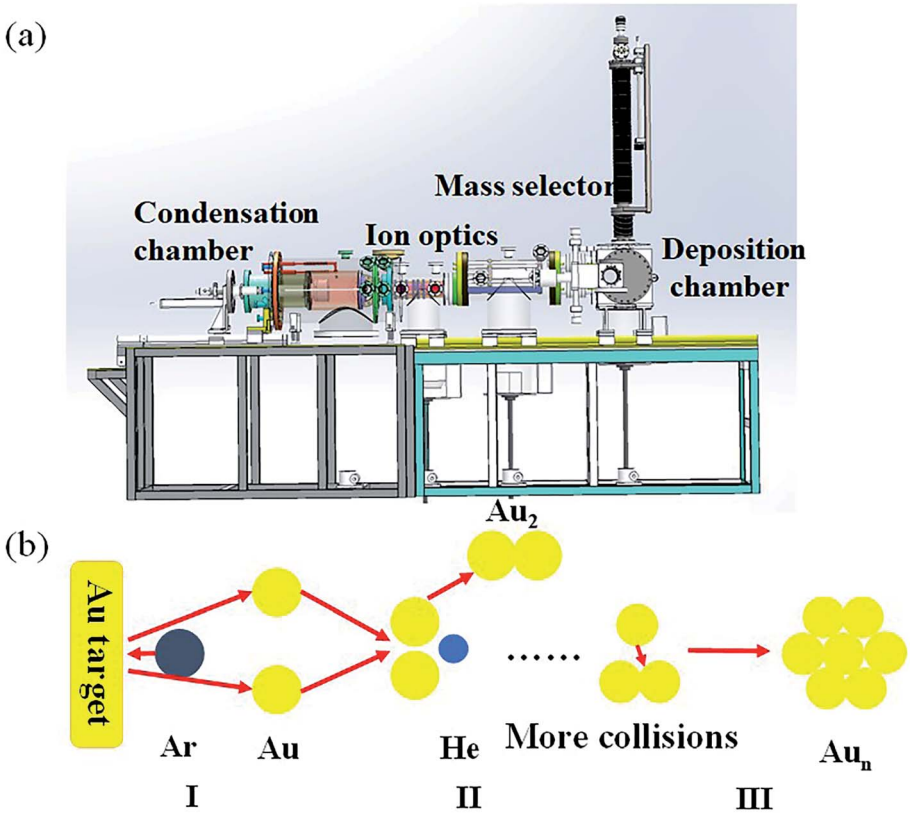


Fig. 1 Schematic of the magnetron sputtering gas-phase condensation cluster source with time-of-flight mass-selector and the formation process of clusters. (a) The schematic of the cluster source. The source is composed of four parts, namely condensation chamber, ion optics, TOF mass selector and the deposition chamber. (b) The formation process of clusters in the condensation chamber. (I) The hot gold atoms (golden) are sputtered out by argon atoms (gray). (II and III) The sputtered atoms are cooled down by multi-body collisions with helium gas (blue) and aggregate with each other.

structure is obtained. By comparing the simulation and experimental images, the structure of each cluster in the STEM image can be assigned. Except for a normally prepared $Au_{923\pm20}$ clusters (group 1) with the highest beam current of about 80 pA, we prepared other three groups of $Au_{923\pm20}$ clusters by changing the preparation conditions from group 1, which are shown in Table 1 below with five sets of condensation parameters. We primarily changed the sputtering power, He gas flow and the condensation length while slightly changing Ar gas to sustain a steady and detectable deposition current. The total pressure in the condensation chamber is changed when we change the helium and argon gas flows.

The yield of the $Au_{923\pm20}$ clusters *versus* the condensation length is shown in Fig. 2(a). The collision times between gold atoms, clusters and helium atoms increases with the condensation length, leading to a higher cluster yield. The mass spectra of small gold clusters and the deposition current of the $Au_{923\pm20}$ clusters *versus* time are shown in Fig. 2(b). For small clusters, there exist discrete mass spectra, while the yields of $Au_2$ and $Au_3$ are 9.13 nA and 6.64 nA, respectively. The inset shows the optimized deposition beam current of the $Au_{923\pm20}$ clusters *versus* time. When we switch off and switch on the mass selection pulse to stop and restart cluster deposition, the beam current shows an obvious decrease to zero, followed by rebound. In this way, we confirm that the deposition current of the $Au_{923\pm20}$ clusters is real rather than the background noise, and the maximum steady deposition current for $Au_{923\pm20}$ is about 80 pA. In Fig. 2(c), the STEM images of the $Au_{923\pm20}$

Table 1 The variation of synthesis conditions for the different structure proportions of $Au_{923\pm20}$ clusters

| Group number | Sputtering power (W) | Helium flow (sccm) | Argon flow (sccm) | Condensation pressure (Pa) | Condensation length (cm) |
|---|---|---|---|---|---|
| 1 | 20 | 154 | 176 | 54 | 27 |
| 2 | 60 | 15 | 184 | 17 | 12 |
| 3 | 80 | 11 | 179 | 16 | 12 |
| 4 | 120 | 11 | 183 | 17 | 12 |

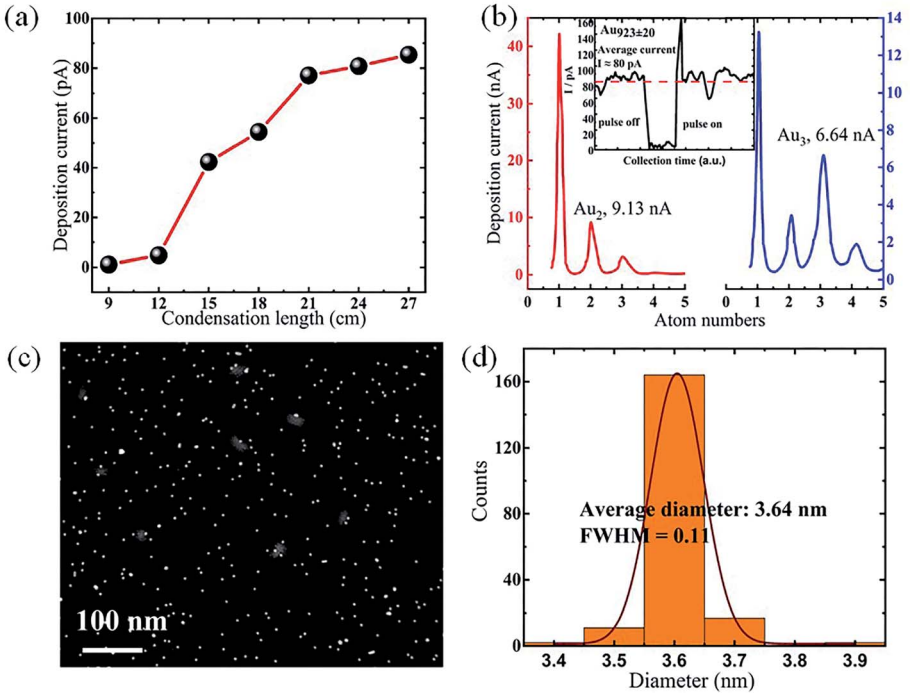


Fig. 2 Influences of the gold cluster yield and the size statistics. (a) The influence of the condensation length on the $Au_{923\pm20}$ cluster yield. The deposition current increases monotonously as the condensation length increases. (b) Yields of gold clusters. The controllable maximum beam current of $Au_2$ and $Au_3$ clusters are 9.13 and 6.64 nA, respectively. The inset shows the maximum steady deposition current of $Au_{923\pm20}$ clusters *versus* time. When we switch off the pulse to stop collection, an obvious decrease in the deposition current from 80 pA to about 0 appears. (c) The uniform distribution of the as-prepared $Au_{923\pm20}$ clusters in the STEM image of in a low magnification. (d) Size statistics of $Au_{923\pm20}$ clusters. The average size is 3.67 nm and the FWHM is 0.11 nm.

clusters with low magnification clearly indicate their uniform spherical shape. The average size is $3.64 \pm 0.11$ nm, as shown in Fig. 2(d), after measuring over 100 clusters. The narrow FWHM with the dense distribution shows that we successfully synthesized the $Au_{923\pm20}$ clusters with a high yield. Three sets of matches between simulated and experimental STEM images for typical structures of the $Au_{923\pm20}$ clusters are shown in Fig. 3(a)–(c). Each simulated structure has some typical characteristics to distinguish from others. Taking Fig. 3(c) for instance, the circular rings with a bright dot in it is a typical feature of the Ih structure in STEM. In this manner, we classify the cluster in Fig. 3(c) as an Ih structure, while the three turns of stripes and the straight stripe distinguish them from each other (Fig. 3(a) and (b)). In Fig. 3(d), the fuzzy STEM image is attributed to either the naturally amorphous structure or the specific angle facing the electron beam cannot match each of the simulated images; therefore, we classify this as an unknown structure. By comparing simulated and experimental images, clusters with different structures observed in STEM are classified and counted. The proportions of the above four structures considerably change in the four groups, as shown in Fig. 4(a)–(d). The dark gray, red, blue and green parts in the pie charts represent Dh, Fcc, Ih and an unknown structure, respectively. In Fig. 4(a), namely, group 1, a statistical result of the normal synthesis condition is observed where the Dh structure occupies a majority of all clusters with a proportion of 65.45%. The Ih structure only accounts for a small part of 10.92%. Moreover, the bulk-favorable cuboctahedron (*i.e.* Fcc) structure only takes a small part of 18.18%. However, in group 2, with a condensation length of 12 cm, the lowest helium gas flow, a sputtering power of 60 W, and an obvious increase of Ih structure from 10.92% to 31.65% were observed. Simultaneously, the Dh

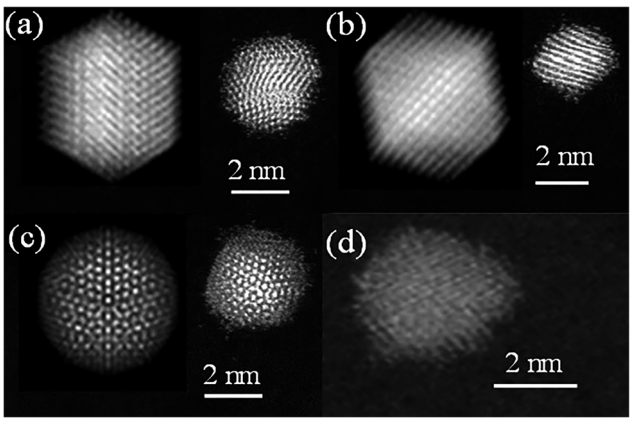


Fig. 3 Comparison between the simulated STEM images and the experimental ones for different structures. (a) On the top left corner is the simulated STEM image of a Dh structure, while the top right one is an experimental result. (b) The simulated STEM image and an experimental result of an Fcc structure. (c) The simulated STEM image and an experimental result of an Ih structure. (d) The experimental STEM images that cannot match with each simulated STEM ones.

 

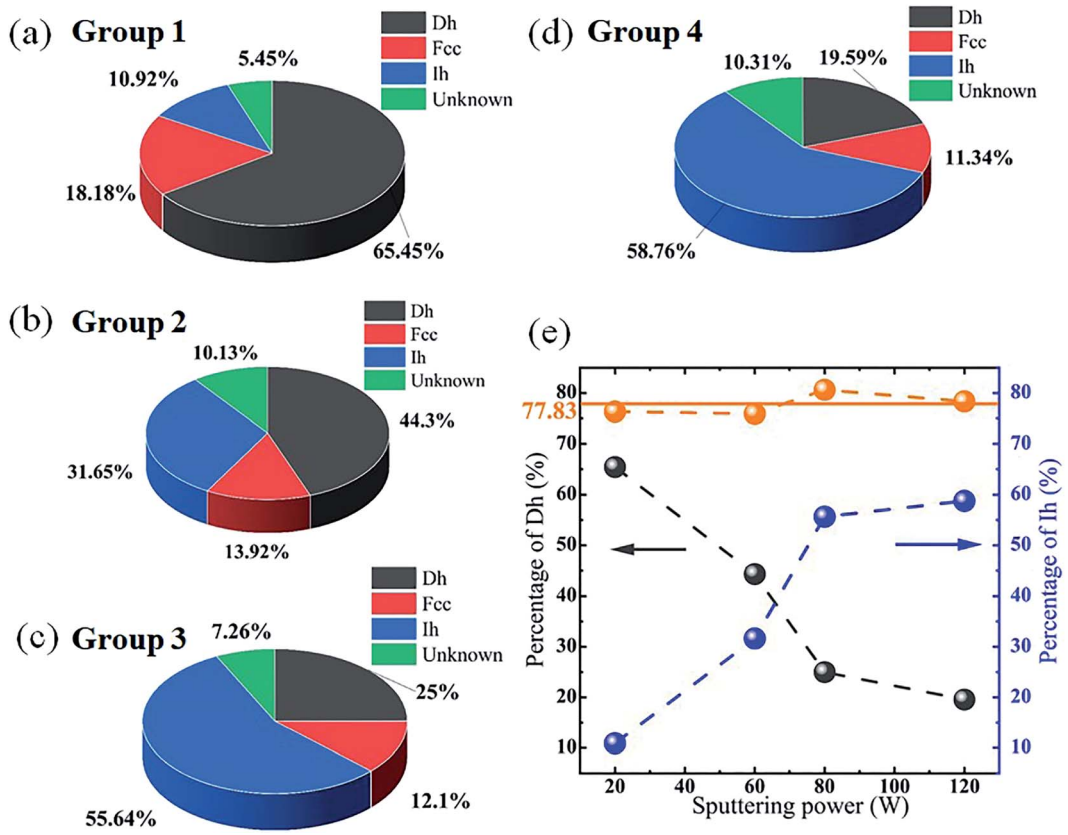


Fig. 4 The structural statistic of the $Au_{923\pm20}$ clusters in different synthesis conditions. (a) The normal synthesis condition for the $Au_{923\pm20}$ clusters with 20 W sputtering power, 27 cm condensation length, and high helium gas flow. (b)–(d) The changed synthesis condition with the lowest helium gas flow and the shortest condensation length of 12 cm. The sputtering power increased from 20 to 60, 80 and 120 W. (e) The dark gray and blue balls refer to the proportion of Dh and Ih structures, while the orange one refers to the sum of proportions of the two structure. The orange-dashed line represents the average proportion of the sum.

structure shows a rapid decrease to 44.3%, which may indicate a structure transformation from Dh to Ih. In this condition, the Fcc structure had a slight decrease to 13.92%. When we continue to increase the sputtering power to 80 W while keeping other parameters almost unchanged, the structure proportion continues to change. As shown in Fig. 4(c), the Ih structure reaches 55.64%, while the Dh structure declines to only 25%. Furthermore, the Fcc structure shows a very slight decrease to 12.1%. When further increasing the sputtering power to 120 W, the transformation to the Ih structure slows down and only reaches 58.76%. In Fig. 4(e) the visualizing trend about the two structures Dh and Ih *versus* different sputtering power is shown. The dark gray and blue balls refer to the proportion of the Dh and Ih structures. The orange one refers to the sum of the proportions of the two structures, while the orange dashed line represents the average proportion of it. It is obvious that the proportions of Dh and Ih structures show considerable changes in a variety of synthesis conditions when the Ih structure rises from 10.92% to 58.76% and the Dh structure falls from 65.45% to 19.59%. Furthermore, we note that the sum of these two structures occupy a quite stable percentage of about 77.83% for all groups. Therefore, it might be possible that the transformation from Dh to Ih is the major process in our structural control.

## Discussion

The yield of clusters with certain atom numbers reaches maximum when we have a suitable condensation condition to control the collision time during the cluster growth. However, the cluster yield is partially limited because only part of atoms aggregates into the (923 ± 20) range. The beam consumption in the chamber occupies a large part in the total loss; therefore, the aerodynamic optimization of chamber is required to effectively guide the beam out of the chamber. As for the structure control, the $Au_{923\pm20}$ clusters prepared in the gas phase are mostly in penta-rotating symmetrical structures (Dh or Ih structures) and the proportion of the sum of these two structures takes up over three quarters. Nevertheless, the proportion of bulk-favorable cuboctahedron structure takes up only 10–20%. It needs further study that at which atom numbers the bulk-favorable structure begin to be the thermodynamically most stable structure. This atom numbers could be a limit for bulk-like Au nanoparticles.[10] The effective structure control indicates that the proportions of different cluster structures are controllable by changing the synthesis condition in the condensation chamber. As shown by previously reported studies,[5,26] the vibrational frequencies in Ih structures are smaller than Dh ones, while Dh structures have softer vibrations than Fcc ones. Considering the entropic

contributions in cluster structure transitions, we can simply make a point that for a given atomic numbers of clusters, Ih structures prefer higher temperature than Dh and Fcc ones. In our experiments, by decreasing the condensation length as well as the flow of helium gas, the collision times of clusters with helium gas decreased, thus the heat carried away from clusters reduced, creating high temperature during cluster growth.[27,28] The increased sputtering power leads to the excessive sputtered energetic gold atoms, which further results in insufficient cooling within the gold atom gas. In this manner, we increase the average temperature of clusters, and the preferred structural transition from Dh to Ih happens. The bulk-favorite Fcc structures are influenced in the same way by the gradually significant entropic contributions. Note that the increased temperature suppresses the previously small proportion of it. These changes lead to an evolution in Dh fractions.[29,30] However, there remain some problems. First, the cluster yield shows a great decrease to several pA when we change the synthesis conditions because the increased temperature, the insufficient helium gas and the shortest condensation length influence the average collision times in the aggregation of atoms,[27,31] creating a harsh environment for the cluster growth, particularly for such a large cluster. Second, the proportion of penta rotation structures is almost invariable, which may indicate that there exists an upper limit in the Ih structure if the most probable structure transforming happens from the Dh to the Ih structure. Finally, the separation[32] and preservation of the metastable clusters[33,34] are needed for further applications. In our study, the structure change during the STEM can easily happen during the irradiation of electron beam.

## Conclusion

In this study, atomically precise $Au_{923\pm20}$ clusters are generated in a gas-phase condensation cluster source equipped with a lateral time-of-flight mass selector. The beam current reaches up to 9.13 nA for small clusters and 80 pA for the $Au_{923\pm20}$ clusters. For $Au_{923\pm20}$, the average size is confirmed by STEM to be $3.64 \pm 0.11$ nm with a narrow distribution FWHM = 0.11 nm. By adjusting the synthesizing conditions in the condensation chamber, we successfully enrich the Ih clusters of size $923 \pm 20$ gold atoms to be the absolute majority from 10.92% to 58.76%, while the original majority Dh structure falls from 65.45% to 19.59%.

## Conflicts of interest

The authors declare no conflict of interest.

## Acknowledgements

We gratefully acknowledge the financial support of the National Key R&D Program of China (2017YFA0303203), the National Natural Science Foundation of China (91622115, 11522432, 11574217, U1732273, U1732159, 61822403, 11874203, 11904165 and 11904166), the Natural Science Foundation of Jiangsu Province (BK20160659), and the Fundamental Research Funds for the Central Universities.

## References

1 T. P. Martin, Shells of atoms, *Phys. Rep.*, 1996, **273**, 199–241.
2 R. L. Johnston, *Atomic and molecular clusters*, CRC Press, 2002.
3 W. A. De Heer, The physics of simple metal clusters: experimental aspects and simple models, *Rev. Mod. Phys.*, 1993, **65**, 611.
4 J. Wang, G. Wang and J. Zhao, Density-functional study of Au n ($n = 2$–2 0) clusters: lowest-energy structures and electronic properties, *Phys. Rev. B: Condens. Matter Mater. Phys.*, 2002, **66**, 035418.
5 F. Baletto and R. Ferrando, Structural properties of nanoclusters: energetic, thermodynamic, and kinetic effects, *Rev. Mod. Phys.*, 2005, **77**, 371.
6 A. Y. Tsivadze, G. Ionova, V. Mikhalko, I. Ionova and G. Gerasimova, The fine structure of plasmon bands in gold nanoparticles, *Prot. Met. Phys. Chem. Surf.*, 2013, **49**, 166–168.
7 H. Häkkinen, M. Moseler and U. Landman, Bonding in Cu, Ag, and Au clusters: relativistic effects, trends, and surprises, *Phys. Rev. Lett.*, 2002, **89**, 033401.
8 S. Bulusu, X. Li, L.-S. Wang and X. C. Zeng, Evidence of hollow golden cages, *Proc. Natl. Acad. Sci. U. S. A.*, 2006, **103**, 8326–8330.
9 J. Li, X. Li, H.-J. Zhai and L.-S. Wang, $Au_{20}$: a tetrahedral cluster, *Science*, 2003, **299**, 864–867.
10 C. L. Cleveland, *et al.*, Structural evolution of smaller gold nanocrystals: the truncated decahedral motif, *Phys. Rev. Lett.*, 1997, **79**, 1873.
11 N. Shao, *et al.*, Probing the Structural Evolution of Medium-Sized Gold Clusters: $Au_n^-$($n$ = 27–35), *J. Am. Chem. Soc.*, 2010, **132**, 6596–6605.
12 Y. Wang, S. Teitel and C. Dellago, Melting of icosahedral gold nanoclusters from molecular dynamics simulations, *J. Chem. Phys.*, 2005, **122**, 214722.
13 D. Foster, T. Pavloudis, J. Kioseoglou and R. Palmer, Atomic-resolution imaging of surface and core melting in individual size-selected Au nanoclusters on carbon, *Nat. Commun.*, 2019, **10**, 1–8.
14 D. Ricci, A. Bongiorno, G. Pacchioni and U. Landman, Bonding trends and dimensionality crossover of gold nanoclusters on metal-supported MgO thin films, *Phys. Rev. Lett.*, 2006, **97**, 036106.
15 Q. Li, D. Yin, J. Li and F. L. Deepak, Atomic-scale understanding of gold cluster growth on different substrates and adsorption-induced structural change, *J. Phys. Chem. C*, 2018, **122**, 1753–1760.
16 K.-J. Hu, *et al.*, Atomic resolution observation of a size-dependent change in the ripening modes of mass-selected Au nanoclusters involved in CO oxidation, *J. Am. Chem. Soc.*, 2015, **137**, 15161–15168.
17 S. R. Plant, L. Cao and R. E. Palmer, Atomic structure control of size-selected gold nanoclusters during formation, *J. Am. Chem. Soc.*, 2014, **136**, 7559–7562, DOI: 10.1021/ja502769v.

18 G. Sun and P. Sautet, Metastable structures in cluster catalysis from first-principles: Structural ensemble in reaction conditions and metastability triggered reactivity, *J. Am. Chem. Soc.*, 2018, **140**, 2812–2820.
19 C. Yu, *et al.*, Optical properties of size selected neutral Ag clusters: electronic shell structures and the surface plasmon resonance, *Nanoscale*, 2018, **10**, 20821–20827.
20 Z. Wang and R. Palmer, Mass spectrometry and dynamics of gold adatoms observed on the surface of size-selected Au nanoclusters, *Nano Lett.*, 2012, **12**, 91–95.
21 Z. Wang and R. Palmer, Determination of the ground-state atomic structures of size-selected Au nanoclusters by electron-beam-induced transformation, *Phys. Rev. Lett.*, 2012, **108**, 245502.
22 B. Von Issendorff and R. Palmer, A new high transmission infinite range mass selector for cluster and nanoparticle beams, *Rev. Sci. Instrum.*, 1999, **70**, 4497–4501.
23 H. Haberland, H. Kornmeier, C. Ludewigt, A. Risch and M. Schmidt, A double/triple time-of-flight mass spectrometer for the study of photoprocesses in clusters, or how to produce cluster ions with different temperatures, *Rev. Sci. Instrum.*, 1991, **62**, 2621–2625.
24 M. Fárník, *Molecular dynamics in free clusters and nanoparticles studied in molecular beams*, ICT Prague Press, Institute of Chemical Technology Prague, 2011.
25 M. Schwartzkopf, *et al.*, From atoms to layers: in situ gold cluster growth kinetics during sputter deposition, *Nanoscale*, 2013, **5**, 5053–5062.
26 J. P. K. Doye and F. Calvo, Entropic effects on the structure of Lennard-Jones clusters, *J. Chem. Phys.*, 2002, **116**, 8307–8317.
27 E. Kesälä, A. Kuronen and K. Nordlund, Molecular dynamics simulation of pressure dependence of cluster growth in inert gas condensation, *Phys. Rev. B: Condens. Matter Mater. Phys.*, 2007, **75**, 174121.
28 E. Blaisten-Barojas and M. Zachariah, Molecular-dynamics study of cluster growth by cluster–cluster collisions, *Phys. Rev. B: Condens. Matter Mater. Phys.*, 1992, **45**, 4403.
29 P. J. Kelly and R. D. Arnell, Magnetron sputtering: a review of recent developments and applications, *Vacuum*, 2000, **56**, 159–172.
30 M. Seah, Universal equation for argon gas cluster sputtering yields, *J. Phys. Chem. C*, 2013, **117**, 12622–12632.
31 S. Pratontep, S. Carroll, C. Xirouchaki, M. Streun and R. Palmer, Size-selected cluster beam source based on radio frequency magnetron plasma sputtering and gas condensation, *Rev. Sci. Instrum.*, 2005, **76**, 045103.
32 T. Suetsuna, *et al.*, Separation of $N_2@C_{60}$ and $N@C_{60}$, *Chem.–Eur. J.*, 2002, **8**, 5079–5083.
33 A. Simo, *et al.*, Formation mechanism of silver nanoparticles stabilized in glassy matrices, *J. Am. Chem. Soc.*, 2012, **134**, 18824–18833.
34 J. F. Hund, *Surface deposition and encapsulation of metallic clusters*, University of Missouri-Rolla, 2004.